Multishot simulations of rime ice accretion

By F. Zabaleta, H. Yu AND P. Moin

This study investigates multishot ice accretion simulations on a NACA 23012 airfoil under rime ice conditions, replicating Case 241 from the 1st Ice Prediction Workshop. We employ wall-modeled large-eddy simulations coupled with a Lagrangian particle model for droplet trajectories and a level-set approach for geometry evolution. To capture local impingement variations from droplet statistics provided only as an expected value, we introduce a stochastic model based on a Poisson point process. The predicted mean ice shapes demonstrate excellent agreement with experimental data, converging towards the laser-scanned profile as the number of shots is increased. However, significant discrepancies in surface roughness characteristics are observed, highlighting the limitations of current multishot methodologies in capturing small-scale features. This research presents the first ice accretion simulations using the charLES solver and forms the basis for future fully coupled simulations to accurately represent the complex interplay between surface roughness development and ice accretion dynamics.

1. Introduction

Ice accretion occurs when supercooled liquid droplets impinge and freeze on aircraft wings and other lift-producing surfaces during flight in subfreezing conditions. Airframe icing represents a persistent hazard to aviation safety, having contributed to numerous accidents and fatalities throughout aviation history. For instance, a review of US aviation incidents from 1982 to 2000 found that airframe icing was a causal factor in 583 accidents, leading to more than 800 fatalities (Petty & Floyd 2004). In the period 2008–2021, an average of five fatalities per year were caused by in-flight icing in the United States (National Transportation Safety Board 2023). The danger of icing stems from its immediate and detrimental impact on aircraft performance. Ice accretion leads to a dangerous combination of increased aerodynamic drag and weight while simultaneously reducing lift. These factors collectively increase the aircraft's stall speed and degrade overall performance, potentially leading to a loss of stable flight (Gent *et al.* 2000).

Two main types of ice can form on aircraft under different ambient conditions: rime and glaze ice. Rime ice generally forms at low flight temperatures ($T < -20°C$), low speeds, low atmospheric liquid water content (LWC), and small droplet sizes (Gent *et al.* 2000). Under rime ice conditions, heat transfer mechanisms are sufficient to remove all the latent heat of solidification from the impinging supercooled droplets, causing them to freeze entirely upon impact. Consequently, under these conditions, the ice geometry is governed predominantly by the droplet impingement distribution and is largely independent of the heat transfer process. Glaze ice tends to form at ambient temperatures closer to the freezing point, at higher speeds, for clouds with elevated LWC and larger droplet sizes. In glaze conditions, only a fraction of the impinging droplets freeze immediately; the remainder form a liquid film that flows downstream along the airfoil, where it either freezes or sheds from the surface. This ice type often has a translucent appearance and can produce protrusions known as horns, which significantly degrade aerodynamic perfor-

mance. In this regime, the ice accretion rate is strongly dependent on the heat transfer process needed to extract the latent heat of solidification from the droplets (Zabaleta *et al.* 2025).

Given the large separation of scales between ice formation and fluid flow, the ice accretion process is simulated as a series of quasi-steady steps. First, the flow around the geometry and the distribution of droplet impingement rate are calculated for the clean airfoil (Ozcer *et al.* 2022; Wright *et al.* 2022). Flow simulations are typically performed using Reynolds-averaged Navier–Stokes (RANS) closures while the droplet transport is modeled using Eulerian or Lagrangian models (Bellosta *et al.* 2023). Using the impingement data and flow field as inputs, mass and energy conservation equations are solved for a thin water film on the surface to predict liquid runback and the local freezing rate (Messinger 1953; Myers 2001). In a single-shot framework, the geometry remains fixed and the aerodynamic and impingement solutions are held constant throughout the accretion process (Wright 2008). In contrast, a multishot approach periodically updates the surface geometry based on the accreted ice, remeshes the domain, and recalculates the flow and droplet collection fields at each step.

Three primary approaches have been proposed to perform the geometry evolution (Bourgault-Cote *et al.* 2017). The most straightforward is the algebraic method, where surface nodes are displaced directly according to the local ice accretion rate. More advanced iterative versions of this method improve volume conservation and resolve intersecting growth lines. Alternatively, the grid-based approach utilizes an orthogonal grid (from either the flow solver or an auxiliary one) to compute the evolution of the frontal surfaces. A third and increasingly common approach is the level-set method (Osher & Sethian 1988), which implicitly tracks the ice front. For instance, Donizetti *et al.* (2023) recently applied a level-set method with adaptive mesh refinement on unstructured grids for multishot simulations.

In this brief, we present multishot simulations of rime ice accretion for Case 241 of the 1st Ice Prediction Workshop. Our approach combines wall-modeled large-eddy simulations (WMLES) with a Lagrangian particle model for droplet trajectories and a level-set method based on a Cartesian grid for geometry evolution. Additionally, we introduce a stochastic model based on a Poisson point process to capture local impingement variations when only statistical data of impingement are available. The numerical methods, including the flow solver and particle-tracking algorithms, are described in Section 2. Section 3 details the geometry evolution algorithm using the level-set approach. The stochastic model for droplet impingement is presented in Section 4. Section 5 outlines the model setup. Results from the simulations, including comparisons with experimental data, analysis of collection efficiency profiles, and a comparison of predicted and experimental surface roughness characteristics, are discussed in Section 6. Section 7 presents the conclusions of this work and outlines future research directions.

2. Numerical model

Simulations are performed using charLES (Brès *et al.* 2018), a finite-volume solver for compressible flows. The solver integrates the filtered Navier–Stokes equations for mass, momentum, and total energy,

$$\frac{\partial \overline{\rho}}{\partial t} + \frac{\partial \overline{\rho} \tilde{u_i}}{\partial x_i} = 0, \tag{2.1}$$

$$\frac{\partial \overline{\rho}\tilde{u}_i}{\partial t} + \frac{\partial \overline{\rho}\tilde{u}_i\tilde{u}_i}{\partial x_i} = -\frac{\partial \overline{p}}{\partial x_i} + \frac{\partial \tilde{\tau}_{ij}}{\partial x_i} - \frac{\partial \tilde{\tau}_{ij}^{sgs}}{\partial x_i}, \tag{2.2}$$

$$\frac{\partial \overline{E}}{\partial t} + \frac{\partial \tilde{u}_i\overline{E}}{\partial x_i} + \frac{\partial \tilde{u}_i\overline{p}}{\partial x_i} = \frac{\partial \tilde{\tau}_{ij}\tilde{u}_i}{\partial x_i} - \frac{\partial \tilde{\tau}_{ij}^{sgs}\tilde{u}_i}{\partial x_i} + \frac{\partial}{\partial x_i}\left(\lambda\frac{\partial \overline{T}}{\partial x_i}\right) - \frac{\partial \tilde{Q}_i^{sgs}}{\partial x_i}, \tag{2.3}$$

where $\overline{(\cdot)}$ and $\tilde{(\cdot)}$ denote filtered and Favre-filtered quantities. Here, u_i is the velocity, p is the pressure, ρ is the density, E is the total energy, T is the temperature, λ is the thermal conductivity, Q_i^{sgs} represents the subgrid heat flux, τ_{ij} is the viscous stress, and τ_{ij}^{sgs} is the subgrid-scale stress tensor, closed via the dynamic Smagorinsky model (Germano *et al.* 1991; Moin *et al.* 1991). The ideal gas law relates pressure, density, and temperature.

The solver employs a five-stage Runge–Kutta scheme for time integration and second-order skew-symmetric spatial discretization that conserves kinetic energy and approximately preserves entropy in the inviscid, adiabatic limit (Honein & Moin 2004; Chandrashekar 2013). An algebraic equilibrium wall model provides wall shear stress at the boundaries (Lehmkuhl *et al.* 2018).

2.1. *Droplet trajectory and collection efficiency*

Droplet trajectories are computed using a one-way coupled Lagrangian framework, appropriate for the dilute droplet concentrations encountered in aircraft icing, where interparticle interactions and feedback to the carrier flow are negligible (Balachandar & Eaton 2010).

Individual particle motion follows from Newton's second law,

$$\frac{dx_{p,i}^k}{dt} = v_{p,i}^k, \tag{2.4}$$

$$m_p^k\frac{dv_{p,i}^k}{dt} = -f_i^k, \tag{2.5}$$

where $x_{p,i}^k$ denotes the position of the k^{th} particle, $v_{p,i}^k$ is its velocity, m_p^k is its mass, and f_i^k is the fluid–particle interaction force. Given the large density ratio (ρ_p/ρ) and the significant velocity scale separation, drag dominates the momentum exchange (Guardone *et al.* 2025). The drag force is modeled using the correlation from Schiller & Naumann (1935). To reduce computational cost, smaller particles are modeled using the discrete parcel method (Drew & Passman 1998), in which a group of particles sharing identical dynamic properties is represented by a single computational particle.

Collection efficiency (β) quantifies the local impingement intensity as the ratio of the droplet mass flux reaching the surface ($\dot{m}_s$) to the freestream mass flux ($\dot{m}_\infty$),

$$\beta = \frac{\dot{m}_s}{\dot{m}_\infty}. \tag{2.6}$$

Particle–surface intersections are detected using the triangle-trajectory intersection algorithm from Möller & Trumbore (2005).

For supercooled large droplet conditions, droplet–surface interactions—including adhesion, bouncing, and splashing—are represented using Wright's (2006) model. This model predicts splashing occurrence and mass redistribution based on the particle properties and impact conditions. Complete details on the particle-tracking implementation, the splashing model, and its validation are provided by Zabaleta *et al.* (2024) and Zabaleta & Moin (2025).

3. Algorithm of geometrical evolution of ice accretion

The droplet collection efficiencies obtained from the Lagrangian particle solver are used to compute the mass deposition rate, $\dot{m}_s = \beta \dot{m}_\infty$, at each location on the geometry. For rime ice conditions, it is assumed that all impinging droplets freeze immediately upon impact. This deposition rate is then used to evolve the geometry in time as part of a two-way coupled, multishot simulation of the ice accretion process.

While several methods exist for evolving the ice front, such as algebraic node displacement or grid-based approaches (Bourgault-Cote *et al.* 2017), this study employs the level-set method (Osher & Sethian 1988). This approach implicitly tracks the ice–air interface using a signed distance function (SDF), ϕ, which is defined as the solution to the eikonal equation

$$|\nabla \phi| = 1, \tag{3.1}$$

subject to the boundary condition $\phi = 0$ on the prescribed lower-dimensional boundary.

A conventional approach to solving this equation on a Cartesian grid involves computing ϕ in a narrow band around the surface (often using an axis-aligned bounding boxes (AABB) tree) and then propagating the solution with a method like the fast marching method (FMM), which has a time complexity of $\mathcal{O}(N \log N)$. To reduce this computational expense, we instead adopt the characteristic/scan conversion (CSC) algorithm (Mauch 2003). The CSC algorithm solves the closest point transform problem for all grid points with an efficient linear time complexity of $\mathcal{O}(N)$. For each grid point, it provides the exact signed distance and identifies the closest surface primitive.

The conventional approach to solving this equation on a Cartesian grid and a non-collocated lower-dimensional surface boundary involves computing ϕ in a narrow band around the triangulated surface (using brute force or the AABB tree), and then propagating the solution, for example, using the FMM. The seeding of N_s narrow-band grid points with M surface primitives with the AABB tree has time complexity $\mathcal{O}(N_s \log M)$, and the FMM has time complexity $\mathcal{O}(N \log N)$. Here, for a reduced time complexity, we use the CSC algorithm (Mauch 2003) with a linear time complexity in both M and N. The CSC algorithm solves the closest point transform problem that outputs, for each Cartesian grid point, the exact signed distance to the triangularized surface up to machine precision, as well as the closest surface primitives, where the collection efficiencies are computed.

This implementation differs from other recent level-set icing models, such as that of Donizetti *et al.* (2023), which used adaptive mesh refinement on an unstructured grid. Here, we use a dedicated Cartesian grid solely for the SDF. This strategy effectively decouples the geometry evolution from the computational fluid dynamics mesh.

Once the SDF is calculated, the ice front is advected in time by solving the level-set advection equation,

$$\frac{\partial \phi}{\partial t} + V \cdot \nabla \phi = 0, \tag{3.2}$$

where the advection velocity, V, is the normal propagation of the wall icing front velocity. Here, the normal velocity propagation method gives $V = V_f \nabla \phi / |\nabla \phi|$, where V_f is the ice front velocity of the closest surface primitive corresponding to the Cartesian grid point (Figure 1(b)). This velocity formula simplifies the advection equation to $\partial \phi / \partial t + V_f = 0$, assuming that the eikonal equation is satisfied for the short duration of one shot. The ice front velocity is computed from the mass collection rate as $V_f = \dot{m}_s / \rho_{ice} A_s$. We note

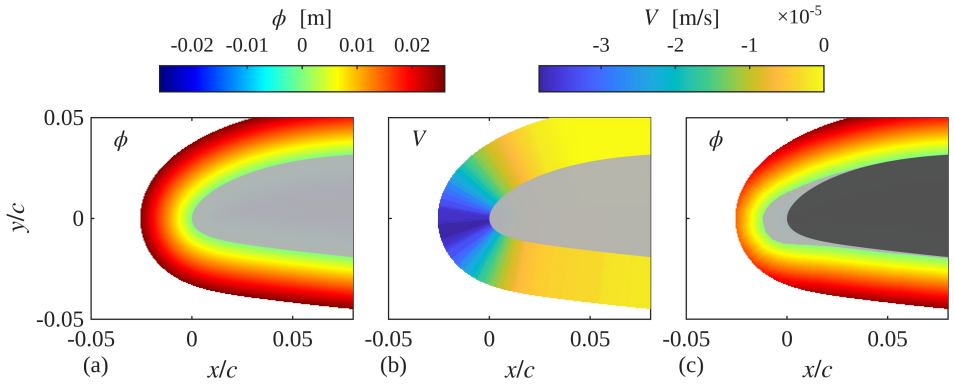

Figure 1: Schematics of the time integration of the ice front with implicit level-set representation. The CSC algorithm computes the signed distance up to a certain normal distance (see (a)), and the advection velocity for the signed distance field is propagated from the wall icing front velocity (see (b)). The explicit surface is constructed with marching cube from the evolved signed distance fields (see (c)).

that this normal propagation of ice front velocity does not preserve the mass of impinged droplets exactly.

Finally, after the SDF is advected for the shot duration, the new explicit ice surface (the $\phi = 0$ isosurface) is constructed using the marching cube algorithm (Lorensen & Cline 1987) implemented in VTK. The entire process is illustrated in Figure 1, for the single-shot demonstration of Case 241 from 1st Ice Prediction Workshop (see Sec. 5 for details).

4. Stochastic model for droplet impingement

A stochastic model is introduced to describe the number of droplet impingements on a collection surface. This model is particularly useful when only statistical data of impingement are available, such as those obtained from RANS or Eulerian particle-tracking models. The number of impingements, $N(t)$, is modeled as a Poisson point process with rate parameter λA_s, where A_s is the surface area and λ is the impingement rate per unit area.

A Poisson point process describes the occurrence of random, independent events in continuous time, assuming a constant average rate and no influence between events. Under this framework, $N(t)$ is nondecreasing, and during any time interval Δt, the number of new impingements follows a Poisson distribution: $N(t + \Delta t) - N(t) \sim \text{Pois}(\lambda A_s \Delta t)$. Furthermore, the numbers of impingements occurring in disjoint time intervals are statistically independent.

Assuming a Poisson counting process, the collection efficiency sampled in the time interval $[t, t + \Delta t]$ is

$$\beta = \frac{m_p(N(t + \Delta t) - N(t))}{\text{LWC}U_\infty A_s \Delta t} = \frac{m_p \text{Pois}(\lambda A_s \Delta t)}{LWCU_\infty A_s \Delta t}, \tag{4.1}$$

where m_p is the mass of an individual droplet. The statistical expectation of this sampled collection efficiency, $E[\beta]$, is $E[\beta] = m_p\lambda/(\mathrm{LWC}U_\infty)$. As the sampling time $\Delta t \to \infty$, the variance $D[\beta] \sim \mathcal{O}(1/\Delta t) \to 0$, and the sampled β will converge in probability to this expected value.

Therefore, to connect the known statistical mean β (obtained from the simulation) to the required rate parameter λ of the stochastic model, we simply rearrange this relationship to solve for λ,

$$\lambda = \frac{\beta \ \mathrm{LWC} \ U_\infty}{m_p}. \tag{4.2}$$

The mass impingement rate from the stochastic model is then given by

$$\dot{m}_s \sim \frac{1}{\Delta t} m_p \mathrm{Pois}(\lambda A_s \Delta t). \tag{4.3}$$

In the case of multiple bins of particles of different mean diameters, the stochastic process is applied independently for each bin with the corresponding m_p and LWC.

The random model introduces stochasticity, especially for larger, less frequent particles. Figure 2 shows the growth height, with and without the model, for Case 241 from the 1st Ice Prediction Workshop (described in Section 5).

Note that the stochastic model is applied independently to each boundary face, which can result in a discontinuous mass distribution. To mitigate this issue and introduce spatial correlation, a Gaussian smoothing filter is applied to the mass rate, $\dot{m}_s$, after each realization. This smoothing process is not merely a numerical step; it can be physically interpreted as modeling the spreading of droplets upon impact, with the width of the Gaussian kernel being correlated to the droplet diameter.

It is important to clarify that the stochastic model described above is not applied to the simulations presented in this brief. The large-eddy simulation, by its nature, provides a high-fidelity, time-resolved realization of the particle impingement process. As the simulation time for each shot is sufficient to capture this inherent stochasticity, the use of an additional statistical model is unnecessary. The utility of this Poisson model, however, lies in its potential application to lower-fidelity simulations (such as RANS or Eulerian approaches) which provide only statistical-mean impingement data and lack a natural source of unsteadiness.

5. Model setup

To validate our model, we simulate Case 241 from the 1st Ice Prediction Workshop. This case corresponds to rime ice accretion on a NACA 23012 airfoil with a chord length of 18 inches at an angle of attack of 2°. The case replicates the experiments by Broeren *et al.* (2018) for case ED1977, which was conducted in the Icing Research Tunnel at NASA's Glenn Research Center. The cloud conditions include an LWC of 0.42 g/m^3 and a median volume diameter of 30 μm, represented by a seven-bin droplet size distribution (described in Table 1). The freestream velocity is 102.8 m/s, the static temperature is −23.0°C, the Reynolds number is 3.8×10^6, and the Mach number is 0.325. The airfoil was exposed to icing conditions for 5 min, after which the resulting ice shape was laser-scanned and digitized.

The computational domain has a length that is seven times the chord length, c, and a span of $1c$. At the inlet the mean freestream velocity was specified, and at the outlet a nonreflective boundary condition was used. Slip boundary conditions were imposed at the

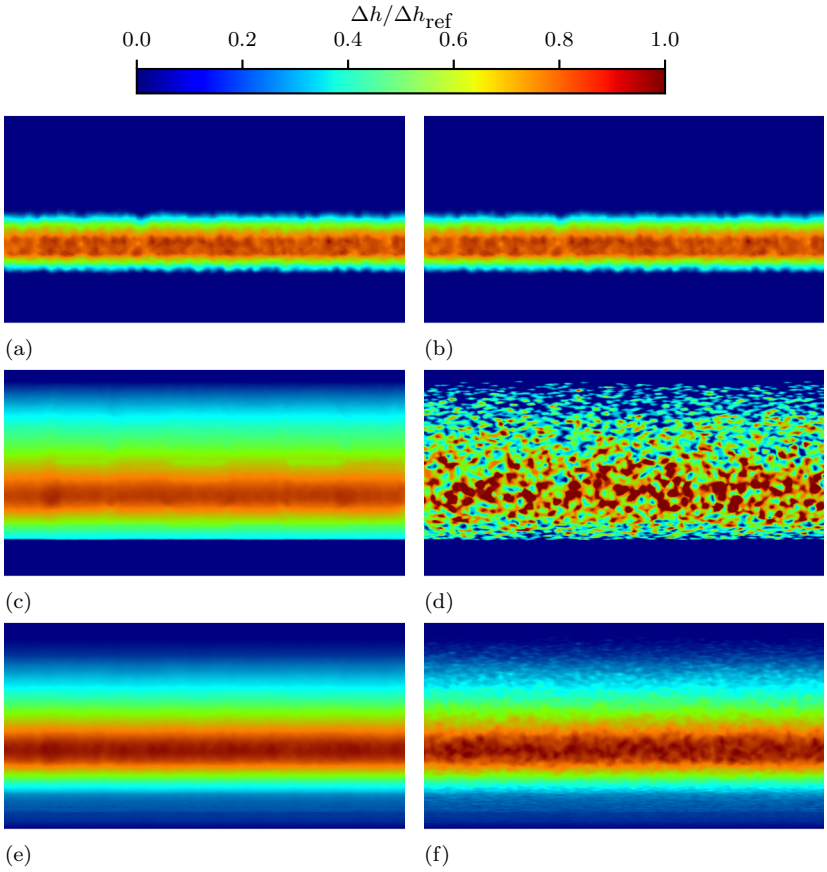

Figure 2: Illustration of the normalized ice accretion height ($\Delta h/\Delta h_{\mathrm{ref}}$) after 2 s for Case 241 from the 1st Ice Prediction Workshop (see Sec. 5 for details). The collection efficiency is computed as statistical mean. (a,b) Growth height due to droplets of mean diameter 6.9 µm without and with the stochastic model, $\Delta h_{\mathrm{ref}} = 2.5 \times 10^{-6}$ m. (c,d) Growth height due to droplets of mean diameter 163.8 µm without and with the stochastic model, $\Delta h_{\mathrm{ref}} = 5 \times 10^{-6}$ m. (e,f) The total height with and without the random model, $\Delta h_{\mathrm{ref}} = 8 \times 10^{-5}$ m.

top, bottom, and spanwise boundaries of the domain. In the spanwise direction, slip conditions rather than periodic boundary conditions were employed because the airfoil loses its spanwise periodicity as ice accretes. For this reason, a large span extent was selected. The computational mesh includes approximately 1150 cells per chord length, sufficient to resolve the flow around a NACA 23012 airfoil at low angles of attack (Bornhoft *et al.* 2024).

Droplets are injected from a rectangular area located $0.5c$ upstream of the airfoil leading edge. The injection area spans the whole domain and has a height of $0.22c$. Each particle is seeded randomly on this area, and particles are eliminated from the domain once they go past the airfoil.

Given the large disparity between the ice accretion timescale and the flow timescale,

Bin	LWC %	Diameter (μm)	m_p (kg)	N_p/m^3	Parcel size	$N_{\mathrm{parcel}}/\mathrm{m}^3$
1	5%	6.9	1.7×10^{-13}	1.2×10^{8}	1000	1.2×10^{5}
2	10%	9.8	4.9×10^{-13}	8.5×10^{7}	1000	8.5×10^{4}
3	20%	14.7	1.7×10^{-12}	5.1×10^{7}	100	5.1×10^{5}
4	30%	30.3	1.5×10^{-11}	8.7×10^{6}	10	8.7×10^{5}
5	20%	60.5	1.2×10^{-10}	7.3×10^{5}	1	7.3×10^{5}
6	10%	100.4	5.3×10^{-10}	7.9×10^{4}	1	7.9×10^{4}
7	5%	163.8	2.3×10^{-9}	9.2×10^{3}	1	9.2×10^{3}

Table 1: Droplet distribution and parcel representation.

simulating the entire 5-min accretion period is computationally prohibitive. While large-eddy simulations of airfoils are typically performed over fractions of a second ($t_{\mathrm{flow}} = c/U_\infty = 0.0044$ s), ice accretion occurs over several minutes. To make these computations affordable, we employ statistical overloading of the cloud, in which the LWC is increased by a fixed factor, thereby reducing the required simulation time by the same factor. This approach is valid only for one-way coupled problems, in which particle–particle interactions and the effect of the dispersed phase on the continuous phase are neglected (Shad *et al.* 2025).

Table 1 presents the seven bins used to describe the droplet cloud, including the number of particles per cubic meter for the given LWC. Most of the particles correspond to the first three bins (approximately 96%), while the last bin represents only 0.003% of the total droplet count (although it accounts for 5% of the total LWC by mass). To achieve faster convergence of β distributions, Zabaleta *et al.* (2024) proposed performing separate simulations for each bin and subsequently combining the results weighted by the percentage of LWC. In this work, because we seek to obtain a single realization of the droplet impingement process, we utilize a different approach. Rather than perform a simulation for each bin, we represent the smaller droplet sizes using particle parcels, in which each Lagrangian particle represents a group of individual droplets traveling together. This approach significantly reduces the computational cost and balances the computational expense introduced by each bin. For the two bins corresponding to the smallest diameters, the parcel size was set to 1000 droplets. For the subsequent five bins, parcel sizes of 100, 10, 1, 1, and 1 were used. These values were selected to ensure that the solution uniformity was not affected by the end of the simulation.

For all the simulations presented in this article, the density of ice was assumed to be constant with a value of $\rho_{\mathrm{ice}} = 917$ kg/m^3.

6. Results

Figure 3 presents compares the ice accretion mean profiles obtained from one-shot and five-shot simulations against the experimental laser-scanned geometry. Both simulations show excellent agreement with the experimental data. The one-shot simulation accurately captures the overall extent and thickness of the ice accretion, although it tends to predict a slightly rounder nose profile. In contrast, the five-shot simulation yields a pointier mean section that more closely aligns with the laser-scanned profile, particularly at the leading

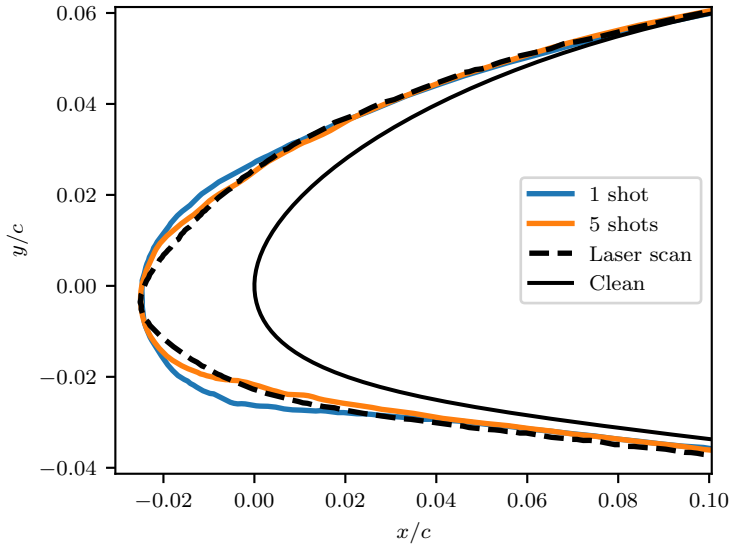

Figure 3: Comparison of simulated mean ice accretion profiles using one and five shots, with laser-scanned experimental data.

edge. The progression from one-shot to five-shot simulations shows a trend toward the laser-scanned profile.

Figure 4 presents the distribution of spanwise averaged collection efficiency (β) along the nondimensional streamwise coordinate (s/c) for five successive simulation shots. Note that the streamwise coordinate represents the projected value on the clean airfoil surface, rather than the actual s value on the accreted shapes. This projection allows for a consistent comparison of equivalent positions as ice accumulates over time. As the ice accretion process progresses through the shots, the β profiles gradually narrow with each successive shot, explaining why single-shot simulations tend to predict rounder ice shapes. In addition, as the number of shots increases, subtle oscillations begin to appear in the β profiles and are especially visible in the fifth shot. These oscillations indicate emerging roughness features in the predicted ice shape, reflecting the simulation's ability to capture the evolving surface irregularities that develop during the accretion process.

6.1. *Roughness comparison*

For rime ice conditions, particularly for this geometry, Bellosta *et al.* (2024) showed that most aerodynamic degradation is attributable primarily to the surface roughness rather than the alteration of the mean ice shape. Therefore, accurate prediction of ice roughness under rime conditions is crucial. Figure 5 compares the roughness distribution maps between the laser-scanned geometry and the five-shot simulation prediction. Despite the excellent agreement in mean shapes, a significant difference is evident in the roughness characteristics of the two surfaces. The laser-scanned geometry exhibits significantly more pronounced roughness features compared with the simulation results. The experimental data show considerable roughness away from the leading edge, particularly on the pressure side. In contrast, the simulation predicts more prominent roughness near the leading edge, albeit with much lower overall magnitude. The simulated roughness features also appear to have longer wavelengths, resulting in a smoother, more gradual variation across the surface.

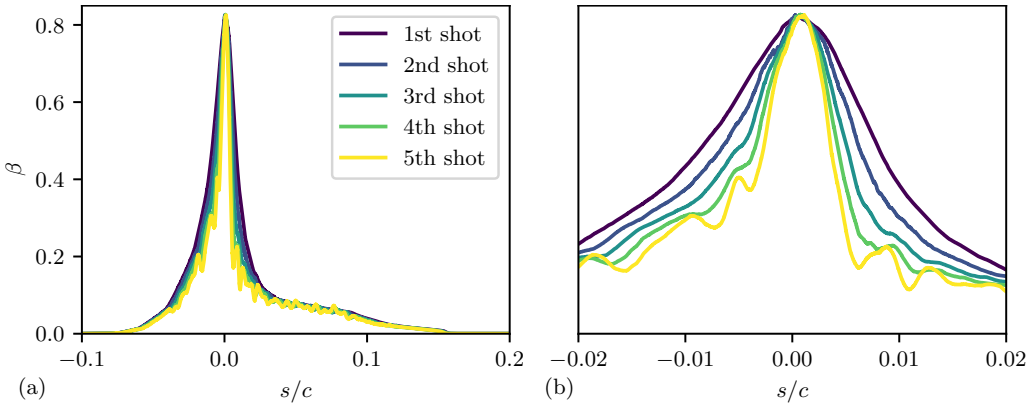

Figure 4: Distribution of spanwise averaged collection efficiency (β) along the nondimensional streamwise coordinate (s/c) for each of five successive simulation shots. Panel (b) shows a magnified view of the stagnation region.

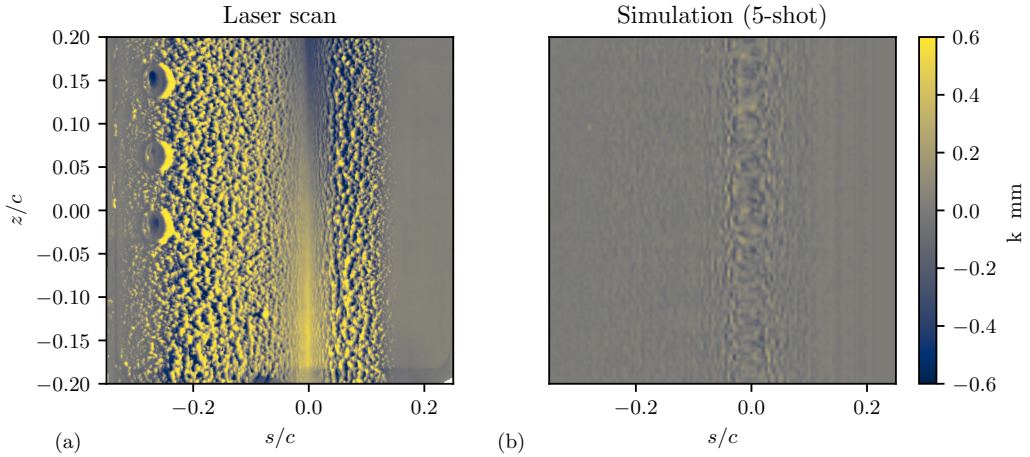

Figure 5: Roughness distribution map for the laser-scanned geometry (a) and predicted from the simulation (b).

This discrepancy in roughness features was expected. While the primary objective of multishot simulations is to account for the feedback between the growing ice and the aerodynamic field, including droplet impact frequency distribution, the time intervals between shots are too long to capture effects at smaller scales. As shown by Zabaleta & Moin (2025), roughness features on the airfoil surface lead to collection efficiency patterns that promote the subsequent growth of these features. The absence of comparable roughness in the final predicted shape could be attributed to overlooking the potential onset of roughness growth between shots and its impact on local collection efficiency distributions. Resolving this issue may require time-resolved simulations that modify the geometry in real time as particles impact the surface, thereby eliminating the quasi-steady assumption. Such an approach would allow for a more accurate representation of the complex interplay between surface roughness development and ice accretion dynamics.

7. Conclusions and next steps

This study presents the first ice accretion simulations using the charLES solver, demonstrating its capability in modeling icing phenomena. Our approach combines WMLES with a Lagrangian particle model for droplet trajectories and a level-set method for geometry evolution in a multishot framework. The novel level-set approach introduced in this work uses the CSC algorithm to compute the exact signed distance from surface tessellation to a Cartesian grid up to a maximum distance with linear computational complexity. The ice front velocities are normally propagated from the surface for the temporal evolutions, and the new, explicit surface, to be fed to the Voronoi-based mesher for the next shot, is reconstructed with the classical marching cube algorithm.

Our results show excellent agreement between both one-shot and five-shot simulations and experimental data for mean ice shapes. The five-shot simulations, in particular, provide a more accurate representation of the ice shape near the leading edge, highlighting the benefits of the multishot approach. However, significant discrepancies are observed in surface roughness characteristics, with simulations underestimating roughness magnitude and spatial distribution. These differences are attributed to the quasi-steady nature of the multishot simulations, which may not fully capture the small-scale dynamics of roughness development between shots.

Additionally, we introduce a stochastic model based on a Poisson point process to capture local impingement variations. While not utilized in the present simulations, this model offers valuable capabilities for scenarios where only expected values of droplet impingement statistics are available, such as in RANS or Eulerian particle-tracking approaches.

Future work will focus on validating the model with additional cases from the Ice Prediction Workshop and developing fully coupled simulations to better capture the onset and growth of surface roughness. These efforts will aim to enhance our understanding of the ice accretion process and improve predictive capabilities for aircraft icing simulations, ultimately contributing to enhanced aviation safety in icing conditions.

Acknowledgments

This investigation was funded by Boeing, NASA's Transformational Tools and Technologies Project. The support of ONR to CTR under grant N000142312833 is gratefully acknowledged. This research used resources of the Oak Ridge Leadership Computing Facility, which is a US Department of Energy, Office of Science, User Facility supported under contract DE-AC0500OR22725. The authors thank Lucy Brown for her insightful comments on this report.

REFERENCES

Balachandar, S. & Eaton, J. K. 2010 Turbulent dispersed multiphase flow. *Annu. Rev. Fluid Mech.* **42**, 111–133.

Bellosta, T., Baldan, G., Sirianni, G. & Guardone, A. 2023 Lagrangian and Eulerian algorithms for water droplets in in-flight ice accretion. *J. Comput. Appl. Math.* **429**, 115230.

Bellosta, T., Donizetti, A., Zabaleta, F., Bornhoft, B., Jain, S. S., Bose, S. T. & Guardone, A. 2024 Assessing relevant roughness scales for accurate prediction of iced airfoil aerodynamics. In *Proceedings of the 2024 Summer Program,* Center for Turbulence Research, Stanford University, pp. 427–437.

Bornhoft, B., Jain, S. S., Goc, K., Bose, S. T. & Moin, P. 2024 Large-eddy simulations of the NACA23012 airfoil with laser-scanned ice shapes. *Aerosp. Sci. Technol.* **146**, 108957.

Bourgault-Cote, S., Hasanzadeh, K., Lavoie, P. & Laurendeau, E. 2017 Multi-layer icing methodologies for conservative ice growth. In *European Conference for Aeronautics and Aerospace Sciences (EUCASS),* pp. 1–15. EUCASS Association.

Brès, G. A., Bose, S. T., Emory, M., Ham, F. E., Schmidt, O. T., Rigas, G. & Colonius, T. 2018 Large-eddy simulations of co-annular turbulent jet using a Voronoi-based mesh generation framework. *AIAA Paper 2018-3302* .

Broeren, A. P., Addy, H. E., Lee, S., Monastero, M. C. & McClain, S. T. 2018 Three-dimensional ice-accretion measurement methodology for experimental aerodynamic simulation. *J. Aircr.* **55**, 817–828.

Chandrashekar, P. 2013 Kinetic energy preserving and entropy stable finite volume schemes for compressible Euler and Navier-Stokes equations. *Commun. Comput. Phys.* **14**, 1252–1286.

Donizetti, A., Rausa, A., Bellosta, T., Re, B. & Guardone, A. 2023 A three-dimensional level-set front tracking technique for automatic multi-step simulations of in-flight ice accretion. In *International Conference on Icing of Aircraft, Engines, and Structures*. SAE International.

Drew, D. A. & Passman, S. L. 1998 *Theory of Multicomponent Fluids*. Springer.

Gent, R. W., Dart, N. P. & Cansdale, J. T. 2000 Aircraft icing. *Philos. Trans. R. Soc. Lond. A* **358**, 2873–2911.

Germano, M., Piomelli, U., Moin, P. & Cabot, W. H. 1991 A dynamic subgrid-scale eddy viscosity model. *Phys. Fluids A* **3**, 1760–1765.

Guardone, A., Bellosta, T., Donizetti, A. & Gallia, M. 2025 Aircraft icing: modeling and simulation. *Annu. Rev. Fluid Mech.* **58**, in press.

Honein, A. E. & Moin, P. 2004 Higher entropy conservation and numerical stability of compressible turbulence simulations. *J. Comput. Phys.* **201**, 531–545.

Lehmkuhl, O., Park, G. I., Bose, S. T. & Moin, P. 2018 Large-eddy simulation of practical aeronautical flows at stall conditions. In *Proceedings of the Summer Program,* Center for Turbulence Research, Stanford University, pp. 87-96.

Lorensen, W. E. & Cline, H. E. 1987 Marching cubes: a high resolution 3D surface construction algorithm. *ACM SIGGRAPH Comput. Graph.* **21**, 163–169.

Mauch, S. 2003 Efficient algorithms for solving static Hamilton-Jacobi equations. PhD thesis, California Institute of Technology, Pasadena, CA.

Messinger, B. L. 1953 Equilibrium temperature of an unheated icing surface as a function of air speed. *J. Aeronaut. Sci.* **20**, 29–42.

Moin, P., Squires, K., Cabot, W. & Lee, S. 1991 A dynamic subgrid-scale model for compressible turbulence and scalar transport. *Phys. Fluids A* **3**, 2746–2757.

Möller, T. & Trumbore, B. 2005 Fast, minimum storage ray/triangle intersection. In *SIGGRAPH '05: ACM SIGGRAPH 2005 Courses*, pp. 1–7. ACM.

Myers, T. G. 2001 Extension to the Messinger model for aircraft icing. *AIAA J.* **39**, 211–218.

National Transportation Safety Board 2023 Aviation accidents: index of months. https://www.ntsb.gov/safety/Pages/research.aspx.

Osher, S. & Sethian, J. A. 1988 Fronts propagating with curvature-dependent speed: algorithms based on Hamilton-Jacobi formulations. *J. Comput. Phys.* **79**, 12–49.

Ozcer, I. A., Aliaga, C., Pueyo, A., Zhang, Y., Fouladi, H., Nilamdeen, S., Selvanayagam, J. & Shah, S. 2022 Ansys—Bombardier 1st Ice Prediction Workshop results. *AIAA Paper 2022-3311* .

Petty, K. & Floyd, C. D. J. 2004 Statistical review of aviation airframe icing accidents in the U.S. In *Proceedings of the 11th Conference on Aviation, Range, and Aerospace Meteorology*. American Meteorology Society.

Schiller, L. & Naumann, A. 1935 A drag coefficient correlation. *Z. Ver. Dtsch. Ing.* **77**, 318–320.

Shad, A., Ahmed, H., Zgheib, N., Balachandar, S. & Sherif, S. A. 2025 Stokes-dependent droplet collection efficiency on a NACA 0012 airfoil from droplet-informed simulations with statistical overloading. *Philos. Trans. R. Soc. Lond. A* **383**, 20240368.

Wright, W. 2006 Further refinement of the LEWICE SLD model. *AIAA Paper 2006-0464* .

Wright, W. 2008 User's manual for LEWICE version 3.2. Tech. Rep., NASA .

Wright, W. B., Porter, C. E., Galloway, E. T. & Rigby, D. L. 2022 GlennICE 2.1 capabilities and results. *AIAA Paper 2022-3309* .

Zabaleta, F., Bornhoft, B., Jain, S. S., Bose, S. T. & Moin, P. 2025 Large-eddy simulations of conjugate heat transfer in boundary layers over laser-scanned ice roughness. *Phys. Rev. Fluids* **10**, 104603.

Zabaleta, F., Jain, S. S., Bornhoft, B. J., Bose, S. & Moin, P. 2024 Large-eddy simulation of supercooled large droplets impingement using a Lagrangian particle approach. *AIAA Paper 2024-4162* .

Zabaleta, F. & Moin, P. 2025 Large-eddy simulations of droplet impingement on iced airfoils. *Annual Research Briefs,* Center for Turbulence Research, Stanford University, pp. 129-141.